THE JOURNAL OF PHYSICAL CHEMISTRY C
A JOURNAL OF THE AMERICAN CHEMICAL SOCIETY

pubs.acs.org/JPCC

Article

H_2 Activation on Pristine and Substitutional ZnO(10$\bar{1}$0) and Cr_2O_3(001) Surfaces by Density Functional Theory Calculations

Jie Luo, Jin-Xun Liu, and Wei-Xue Li*

Cite This: *J. Phys. Chem. C* 2022, 126, 9059−9068

Read Online

ACCESS | Metrics & More | Article Recommendations | Supporting Information

ABSTRACT: As a major component of syngas (a mixture of hydrogen and carbon monoxide), activation of hydrogen molecules on metal oxides plays a vital role in various hydrogenation reactions and synthesis of valuable chemicals. Herein, we present a density functional theory investigation of H_2 activation and subsequent dehydration over pristine and substituted ZnO(10$\bar{1}$0) and Cr_2O_3(001) surfaces. An ab initio thermodynamics study shows that Cr_1 substitution on ZnO(10$\bar{1}$0) and Zn_1 substitution on Cr_2O_3(001) are stable in a wide range of temperatures and pressures. The binding strength of H to the low-valent Zn cations is the weakest one, followed by the high-valent Cr cation and the lattice oxygen coordinated to Cr as wells as to Zn. Heterolytic dissociation is found to be preferential than the homolytic one. The pristine ZnO(10$\bar{1}$0) is active for H_2 dissociation, and the presence of Cr_1 increases the formation energy of oxygen vacancies and lowers the reactivity to H_2 dissociation. Although Cr_2O_3(001) is less active for H_2 dissociation, the presence of Zn_1 lowers the formation energy of oxygen vacancies and promotes the surface reactivity even higher than that of pristine ZnO(10$\bar{1}$0). The dissociated H species turn to recombine and form H_2 rather than reacting with the lattice oxygen to form H_2O. The present work provides a deeper insight into H_2 activation over pristine and heterometal-atom-modified oxide surfaces and a rationale for the design of active catalysts for syngas conversion.

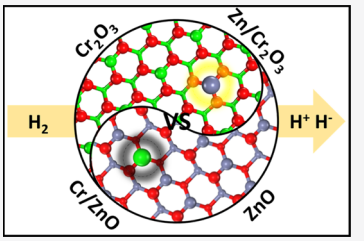

1. INTRODUCTION

Syngas (a mixture of CO and H_2) is a key platform for energy conversion by the utilization of carbon resources,[1] such as natural gas,[2] shale gas,[3] coal,[4] and biomass.[5] Transition-metal oxides play an important role in syngas conversion. Recently, Bao and co-workers developed a bifunctional catalyst consisting of $CrZnO_x$ oxides and MSAPO zeolite (OX-ZEO), using which a selectivity of as high as 80% of light olefins can be achieved for syngas conversion.[6] In fact, various OX-ZEO catalysts, such as ZnO−ZrO_2/SAPO-34,[7] ZnO−Al_2O_3/SAPO-34,[8] Zn−Cr/SAPO-34,[9] $Zn_aMn_bO_x$/ZSM-22,[10] and ZrO_2−In_2O_3/SAPO-34,[11] have been reported to show high selectivity to light olefins and other products. Different from transition-metal catalysts, the bifunctional OX-ZEO catalysts separate the activation of syngas on the oxide part from the subsequent carbon chain growth and hydrogenation on the zeolite part. For the oxide part, the metal−oxide mixtures and/or complex metal oxides were found to be more active than the separated metal oxides.[12−15] Identification of the active sites and their role in syngas conversion remain challenging.[16−18] Mechanistic investigation and gaining an understanding of the intrinsic activity of prototype oxides such as ZnO and Cr_2O_3 for syngas activation and the influence of the defects such as heterometal atoms are valuable for understanding the mechanism behind this phenomenon but not well explored yet.

H_2 activation and adsorption is the first step during the syngas conversion. H_2 dissociation on metal surfaces was extensively investigated before.[19] In Fischer−Tropsch synthesis (FTS) and methanol synthesis reactions catalyzed by Fe,[20,21] Co,[22−24] Ru,[25,26] and Cu[27−29] metals, H_2 readily dissociates homolytically on the metal surfaces to form chemically similar hydrogen atoms, which would recombine to form H_2 molecules and desorb from the surface at higher temperatures. In contrast, on oxide surfaces, H_2 could dissociate heterolytically to form hydride (H^-) and proton (H^+) species coordinating to the metal cation and oxygen anion, respectively. For example, H_2 favors the heterolytic dissociation on the CeO_2(111) surface and then the heterolytic (H^- and H^+) products can further evolve into the homolytic one ($2H^+$).[30] H_2 dissociation on ZnO surfaces was studied before.[31−36] Using scanning tunneling microscopy and density functional theory (DFT) calculations, Shao and co-workers found that the H_2 molecules dissociate heterolytically on ZnO(10$\bar{1}$0) and grow into a one-dimensional chain along the [0001] direction, which can be observed under cryogenic conditions below 55 K.[31] However, most of the hydrogenation reactions occur above room temperature and at even higher temperatures. The presence of heterometal atoms was found to enhance the adsorption of substrates.[37] It is therefore

Received: April 15, 2022
Published: May 20, 2022

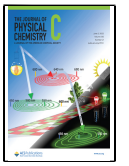

https://doi.org/10.1021/acs.jpcc.2c02607
J. Phys. Chem. C 2022, 126, 9059−9068

interesting to study the influence of heterometal atoms on activation of hydrogen molecules. Cr_2O_3 was widely studied in the field of molecular adsorption and reactions using DFT before, such as adsorption of carbon dioxide[38] and hydrogen sulfide,[39] catalytic oxidation of nitric oxide,[40] and the oxygen reduction reaction.[41] However, compared to ZnO, investigation of hydrogen activation on Cr_2O_3 as well as the influence of heterometal atoms has not been reported yet. Finally, different from transition metals, at higher temperatures, the dissociated products might recombine to form H_2 or react with the lattice oxygen to form H_2O with oxygen vacancies left. Investigation on how these two paths compete as well as their dependence on oxides are valuable for subsequent hydrogenation.

Herein, we systematically investigated H_2 dissociation on the prototype oxide surfaces used in the OX-ZEO catalysts, nonpolar ZnO($10\bar{1}0$) and Cr_2O_3(001), using DFT calculations. To facilitate a consistent comparison with respect to transition metals, we included the corresponding H binding energy from our DFT calculations. The difference between the two oxides provides a critical understanding on the influence of the chemical composition, valence states, and structure on H_2 dissociation. Formation of heterometal atoms, Cr_1 substitution in the surface Zn lattice of ZnO($10\bar{1}0$), and Zn_1 substitution in the surface Cr lattice of Cr_2O_3(001), and their influence on H_2 dissociation were studied in detail. In this work, both heterolytic and homolytic H_2 dissociations over the pristine and substituted ZnO($10\bar{1}0$) and Cr_2O_3(001) were calculated. In addition to recombination and formation of H_2 molecules, dehydration was investigated.

2. THEORETICAL CALCULATIONS

2.1. Density Functional Theory Calculations. DFT[42,43] calculations were performed using the Vienna ab initio simulation package (VASP) with the projector augmented wave[44,45] method. We used the generalized gradient approximation (GGA) applying Perdew−Burke−Ernzerhof functionals.[46] The plane-wave basis set with a kinetic energy cutoff of 400 eV was used to solve the Kohn−Sham equations. The ZnO($10\bar{1}0$) surface was modeled by a three double-layer slab with a (3 × 2) periodicity separated by 12 Å vacuum along the *Z*-direction. To model the Cr-substituted ZnO($10\bar{1}0$) surface, one of the six surface Zn cations is substituted by the Cr cation. The Monkhorst−Pack scheme for a (2 × 2 × 1) k-point mesh was used to sample the Brillouin zone. The two topmost layers of the slab and the adsorbates were relaxed with the residual forces less than 0.02 eV/Å throughout the present work unless mentioned otherwise. GGA calculations were performed on H_2 activation on the ZnO($10\bar{1}0$) surface. Previous calculations showed that GGA + *U* with different *U* values from 2.0 to 6.0 eV applied to the Zn 3d states gives essentially the same adsorption energies and reaction barriers over the ZnO surface with standard GGA.[37,47−49] It is likely that its hybridization with reactants has been little affected due to the nature of the deep-lying Zn 3d states. The optimized lattice constants of bulk wurtzite ZnO are $a = b = 3.29$ Å with $c = 5.30$ Å, which are consistent with the previous experimental results ($a = b = 3.25$ Å with $c = 5.21$ Å).[50,51] The crystal orbital Hamilton population (COHP) method[52,53] was used in chemical bonding analyses as implemented in the LOBSTER package.[54,55]

The Cr_2O_3(001) surface was modeled by four Cr_2O_3-unit layers with a supercell of (2 × 2). The neighboring slabs were separated by 12 Å vacuum layers along the *Z*-direction. To model the Zn-substituted Cr_2O_3(001) surface, one of the four surface Cr cations is substituted by the Zn cation. The bulk Cr_2O_3 in an antiferromagnetic configuration is found to be stable[40,56] and is adopted in the present work. To describe the strong electron correlation of Cr, DFT + *U* was applied to the Cr 3d states with a *U* value of 3 eV.[40,57−59] For the slab model, a Monkhorst−Pack (2 × 2 × 1) k-point mesh was used to sample the Brillouin zone. The plane-wave basis set with a kinetic energy cutoff of 450 eV was used to solve the Kohn−Sham equations. The optimized lattice constants of bulk hexagonal corundum Cr_2O_3 are $a = b = 5.03$ Å with $c = 13.77$ Å, in line with the previous experimental results ($a = b = 4.96$ Å with $c = 13.60$ Å).[60−62]

For comparison, we also studied the bcc Fe(100), hcp Co($10\bar{1}0$), and Zn($10\bar{1}0$) surfaces, which were modeled by a 4-layer slab model with a (2 × 2) supercell separated by 15 Å vacuum along the *Z*-direction. The two topmost layers of the slab and the adsorbates were relaxed with the residual forces less than 0.02 eV/Å. A (4 × 4 × 1) k-point mesh was used to sample the Brillouin zone. The plane-wave basis set with a kinetic energy cutoff of 400 eV was used to solve the Kohn−Sham equations.

The climbing-image nudged elastic band[63] method was used to locate the transition states (TSs). The relaxations stopped when the residual forces on each atom, which were allowed to relax, became smaller than 0.05 eV $Å^{-1}$, and they were verified to possess only one vibrational mode with a negative curvature in the direction of the bond breaking or forming process. The reaction energy and activation energy barriers were calculated using $\Delta E = E_{FS} - E_{IS}$ and $E_{ac} = E_{TS} - E_{IS}$, in which the E_{IS}, E_{FS}, and E_{TS} are the total energy of the initial state (IS), final state (FS), and the corresponding TS without zero-point correction, respectively.

The binding strength of H atoms, E_b, is evaluated using the so-called binding energies below

$$E_b = E_{slab}(H) - E_{slab} - E_{tot}(H)$$

in which E_{slab} and $E_{slab}(H)$ are the total energies of the (metal oxide or metal) slab without and with an adsorbed H atom and $E_{tot}(H)$ is the total energy of the H atom in the gas phase. The dissociative adsorption energy per H_2 molecule E_{ad} is given by

$$E_{ad} = E_{slab}(2H) - E_{slab} - E_{tot}(H_2)$$

where $E_{slab}(2H)$ and $E_{tot}(H_2)$ are the energies of the dissociative adsorbed hydrogen surface and H_2 in the gas phase, respectively. Oxygen vacancy formation energy, E_V, can be calculated using

$$E_V = E_{slab}(O_V) + \frac{1}{2}E_{tot}(O_2) - E_{slab}(\text{oxide})$$

in which $E_{slab}(O_V)$ and E_{slab}(oxide) are the total energies of an optimized oxide slab with and without oxygen vacancies, respectively, and $E_{tot}(O_2)$ is the total energy of an oxygen molecule in the gas phase. Here, a positive number means the corresponding process is endothermic, and a negative number means it is exothermic unless mentioned otherwise.

2.2. Ab Initio Thermodynamics. To evaluate the stability of Cr defects in ZnO, the Gibbs free energy of formation $\Delta G(T,p)$ for Cr substitution in the Zn lattice of Zn($10\bar{1}0$) was investigated. Here, the substituted Zn was in equilibrium with the reservoir of bulk ZnO, introduced Cr was taken from the reservoir of bulk Cr_2O_3, and extra oxygen was consumed by

https://doi.org/10.1021/acs.jpcc.2c02607
J. Phys. Chem. C 2022, 126, 9059−9068

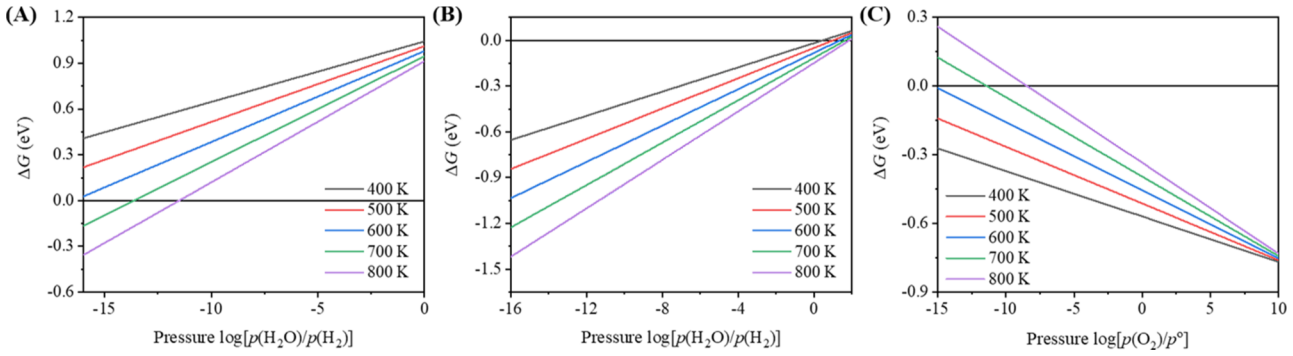

Figure 1. Gibbs free energy of formation $\Delta G(T,p)$ for the Cr substitution on Zn(10$\bar{1}$0) as a function of $p(H_2O)/p(H_2)$ and temperatures with respect to the pristine (A) and defective (B) Zn(10$\bar{1}$0). Gibbs free energy of formation $\Delta G(T,p)$ for the Zn substitution on Cr_2O_3(001) as a function of $p(O_2)$ and temperatures with respect to the pristine Cr_2O_3(001). For the Cr substitution on Zn(10$\bar{1}$0), one of the six surface Zn cations is substituted by the Cr cation. For the Zn substitution on Cr_2O_3(001), one of the four surface Cr cations is substituted by the Zn cation.

H_2(g) in forming H_2O(g) under the reaction conditions. Specifically, corresponding $\Delta G(T,p)$ can be calculated using[64,65]

$$\Delta G(T,p) = E_{ZnO}^{bulk} + E_{Cr/ZnO}^{slab} - \frac{1}{2}E_{Cr_2O_3}^{bulk} - E_{ZnO}^{slab} + \frac{1}{2}(\mu_{H_2O} - \mu_{H_2})$$

where E_{ZnO}^{bulk} and $E_{Cr_2O_3}{}^{bulk}$ are the total energies of the bulk ZnO and Cr_2O_3 and $E_{Cr/ZnO}^{slab}$ and E_{ZnO}^{slab} are the total energies of the Cr-substituted Zn(10$\bar{1}$0) and the pristine Zn(10$\bar{1}$0). T and p dependence is given as $\mu_{H_2O} - \mu_{H_2}$

$$\mu_{H_2O} - \mu_{H_2} = E_{H_2O}^{total} - E_{H_2}^{total} + \tilde{\mu}_{H_2O}(T,p_0) - \tilde{\mu}_{H_2}(T,p_0) + RT\ln\left(\frac{p_{H_2O}}{p_{H_2}}\right)$$

where $\tilde{\mu}$ includes the contribution from rotations and vibrations of the molecule, as well as the ideal-gas entropy at 1 atm, which was calculated using VASPKIT[66] here. p_{H_2O} and p_{H_2} are the partial pressures of water and hydrogen molecules. As shown in Figure 1A, at a low $p(H_2O)/p(H_2)$ ratio and elevated temperatures, corresponding formation energy is exothermic, indicating that the formation of Cr-defects upon substitution is a thermodynamic process likely.

Previous studies show that the synthesized Zn(10$\bar{1}$0) surface might exhibit considerable defects.[67,68] Assuming that there are vacancies of the Zn−O pair with a total energy of E_{ZnO}^{slab-d}, the corresponding Gibbs free energy of formation for Cr in the Zn lattice became

$$\Delta G(T,p) = E_{Cr/ZnO}^{slab} - \frac{1}{2}E_{Cr_2O_3}^{bulk} - E_{ZnO}^{slab-d} + \frac{1}{2}(\mu_{H_2O} - \mu_{H_2})$$

As shown in Figure 1B, on the defective Zn(10$\bar{1}$0), the Cr substitution happens in a wide range of temperatures and partial pressures considered. Indeed, recent studies have already reported the Cr substitution on Zn(10$\bar{1}$0).[69]

To evaluate the stability of the Zn-defects in Cr_2O_3, the Gibbs free energy of formation for the Zn substitution in the Cr lattice of Cr_2O_3(001) was investigated. Here, the substituted Cr was in equilibrium with the reservoir of bulk Cr_2O_3, the introduced Zn was taken from the reservoir of bulk ZnO, and missing oxygen was taken from the reservoir of O_2(g). Specifically, corresponding $\Delta G(T,p)$ can be calculated using

$$\Delta G(T,p) = \frac{1}{2}E_{Cr_2O_3}^{bulk} + E_{Zn/Cr_2O_3}^{slab} - E_{ZnO}^{bulk} - E_{Cr_2O_3}^{slab} - \frac{1}{4}\left(E_{O_2}^{total} + \tilde{\mu}_{O_2} + RT\ln\left(\frac{p_{O_2}}{p^0}\right)\right)$$

where $E_{Zn/Cr_2O_3}{}^{slab}$ and $E_{Cr_2O_3}{}^{slab}$ are the total energies of the Zn-substituted and the pristine Cr_2O_3(001), respectively. As shown in Figure 1C, the Zn substitution in Cr_2O_3(001) is thermodynamically favorable in a wide range of temperatures and partial pressures considered.

3. RESULTS AND DISCUSSION

3.1. H Atom Binding to ZnO(10$\bar{1}$0) and Cr_2O_3(001).

We first calculated H binding strength over various transition metals at 0.25 ML and oxide surfaces to see their difference (Figure 2). On transition metal surfaces, H_2 molecules dissociate into two homolytic H atoms, which have a similar coordination and chemical state.[70,71] Fe and Co, the commonly used metal catalysts in FTS, bind H atoms strongly at the hollow sites with E_b equal to −2.60 eV (exothermic) for Fe(100) and −2.71 eV for Co(10$\bar{1}$0) (Figure S1), whose binding strength is stronger than that of the gas-phase H_2(g) (−2.26 eV). This shows that Fe and Co metal surfaces dissociate H_2 exothermically, when they were as widely used as the FTS catalysts. However, the H atom on Zn(10$\bar{1}$0) has a binding energy of −2.04 eV, and the weak binding strength makes the H_2 dissociative adsorption on Zn(10$\bar{1}$0) endothermic, mainly due to full occupation of the Zn 3d band far from the Fermi level.

Different from the metal surfaces, H atoms on oxide surfaces can bind to metal cations or oxygen anions forming H^- and H^+ species, respectively. Here, we investigate nonpolar ZnO(10$\bar{1}$0), the most stable and abundant facet of wurtzite ZnO.[72,73] The H atom binds to Zn^{2+} and forms H^- species with a binding energy of −0.66 eV, which is extremely weak even compared to the Zn metal. This indicates that the formation of hydride on ZnO alone is unstable. However, the H atom binds to O^{2-} and forms H^+ with a value of −2.69 eV. The binding strength is much stronger than that of H^- to Zn^{2+} by 2.03 eV, and even close to those of the Fe and Co metals.

https://doi.org/10.1021/acs.jpcc.2c02607
J. Phys. Chem. C 2022, 126, 9059−9068

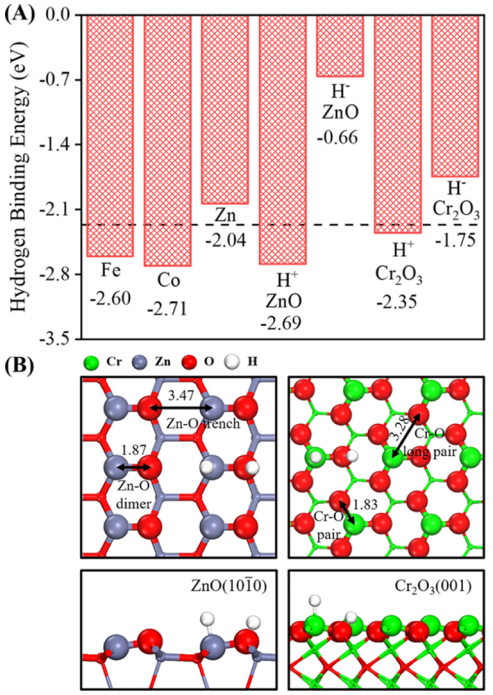

Figure 2. (A) Binding energies of H^+ and H^- ions on $Cr_2O_3(001)$ and ZnO(10$\bar{1}$0) calculated with respect to the isolated H atom. The binding energies of the H atom on Fe(100), Co(10$\bar{1}$0), and Zn(10$\bar{1}$0) are given as a comparison. The dashed line indicates H binding energy in gaseous H_2. The optimized H^+ and H^- ions' adsorption configurations are given in Figure S1. (B) Atomic surface structures and a schematic diagram of hydrogen adsorption of ZnO(10$\bar{1}$0) and $Cr_2O_3(001)$. Green, gray, red, and white spheres represent Cr, Zn, O, and H atoms, respectively.

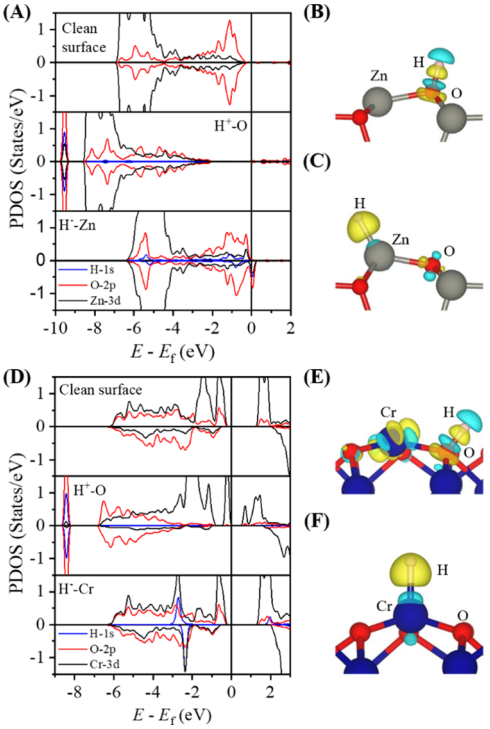

Figure 3. (A) Projected density of states (PDOS) on Zn 3d, O 2p, and H 1s for the clean ZnO(10$\bar{1}$0) surface, H^+/Zn(10$\bar{1}$0), and H^-/ZnO(10$\bar{1}$0); (B,C) charge density difference for H^+/Zn(10$\bar{1}$0) and H^-/ZnO(10$\bar{1}$0) (the isosurfaces of 0.015 au), respectively. (D) PDOS on the Cr 3d, O 2p, and H 1s bands for clean $Cr_2O_3(001)$, $H^+/Cr_2O_3(001)$, and $H^-/Cr_2O_3(001)$. (E,F) Charge density difference for $H^+/Cr_2O_3(001)$ and $H^-/Cr_2O_3(001)$ (the isosurfaces of 0.015 au), respectively. Blue and yellow isosurfaces indicate charge depletion and accumulation.

For hexagonal corundum Cr_2O_3, we investigated the Cr-terminated (001) surface, one of the most exposed surfaces.[59,74] Calculated binding energy of the H atom to the exposed Cr^{3+} forming H^- is −1.75 eV. Though the binding strength is stronger than that to Zn^{2+} by 1.09 eV, it remains weak compared to the Zn metal. The H^+ binding energy to O^{2-} of Cr_2O_3 (001) is −2.35, 0.34 eV weaker than the counterpart of ZnO(10$\bar{1}$0). This makes the binding difference between H^+ and H^- on $Cr_2O_3(001)$ as small as 0.60 eV. These differentiate two oxide surfaces studied as shown more clearly below.

For H atom binding to the lattice oxygen and the Zn cation of ZnO(10$\bar{1}$0), the corresponding Bader charges are +0.41 and −0.28 |e|, indicating formation of H^+ and H^-, respectively. However, the presence of H^+ and H^- has little influence on the Bader charge of coordinated oxygen and Zn and the corresponding Zn−O bond length. On the other hand, the PDOS (Figure 3A) shows that the presence of H^+ and H^- upshifts and downshifts the corresponding Fermi level. This indicates that the electrons are delocalized on the whole surface, rather than localizing on the coordinated O and Zn, though there are certain electron polarizations seen from the charge density difference (Figure 3B,C). For H binding to $Cr_2O_3(001)$, calculated Bader charges for H^+ and H^- are +0.35 and −0.42 |e|, respectively. The electron distributions are very different from those of ZnO. First, the presence of H^+ lowers the valence state of the neighbor Cr cation from +1.76 to +1.47 |e|, and the corresponding Cr−O bond length increases from 1.83 to 2.05 Å. PDOS (Figure 3D) and charge density differences (Figure 3E) further show a significant change in orbital hybridization between Cr and O and charge transfer. This states clearly that the electrons are localized in coordinated Cr and O, in stark contrast to ZnO.

3.2. H_2 Activation on Pristine and Cr_1-Substituted ZnO(10$\bar{1}$0). H_2 molecular adsorption over ZnO(10$\bar{1}$0) has a small exothermic energy of −0.09 eV and falls well in the range of physical adsorption. Subsequent H_2 activation via both homolytic and heterolytic pathways was studied on the pristine ZnO(10$\bar{1}$0). For homolytic activation, the two dissociative H atoms bound with two adjacent Zn cations are highly endothermic with E_{ad} equal to 3.28 eV/H_2, and the corresponding dissociation process cannot happen. When two dissociative H atoms were bound with two adjacent O anions, the corresponding E_{ad} becomes slightly exothermic and is equal to −0.15 eV/H_2. Considering the large separation distance of 3.28 Å between two anions with respect to the H−H bond length of 0.75 Å in the gas phase, large H−H bond stretching is required to reach the TS of dissociation. This would result in a large dissociation barrier and therefore cannot be calculated explicitly.

The heterolytic splitting of H_2 generates one H^- bound to the Zn cation and one H^+ bound to the O anion. This can take place over the Zn−O dimer or Zn−O trench along the [0001] direction as indicated in Figure 2B. The corresponding E_{ad} values are −0.48 eV/H_2 and −0.24 eV/H_2, respectively. For the former one, the calculated Bader charges are −0.36 |e| for H^- and 0.39 |e| for H^+. Accordingly, the heterolytic

https://doi.org/10.1021/acs.jpcc.2c02607
J. Phys. Chem. C 2022, 126, 9059−9068

dissociations are exothermic and energetically feasible on ZnO(10$\bar{1}$0). When H^- and H^+ are separated by an infinitely large distance, the corresponding E_{ad} becomes highly endothermic and is equal to 1.17 eV/H_2. This indicates a strong lateral attraction between H^+ and H^-, which is, however, not found in Cr_2O_3(001) below. COHP analysis (Figure 4) shows that with the presence of H^+ nearby, there is

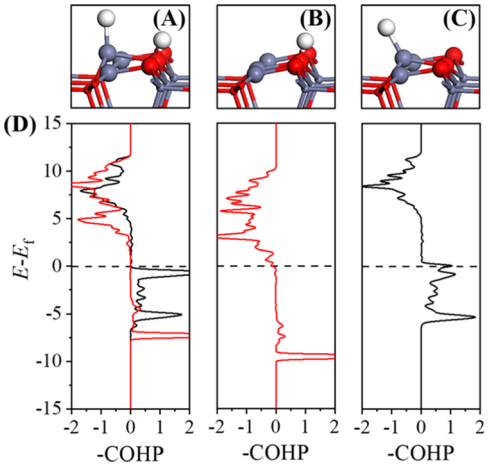

Figure 4. (A) H_2 heterolytic dissociative adsorption configuration over the Zn−O dimer, (B) H^+ and (C) H^- adsorption configurations on ZnO(10$\bar{1}$0), and (D) corresponding COHP curves.

more bonding orbital populated on H^-, and the Bader charge increases from −0.28 |e| to −0.36 |e|. The electrostatic attraction of H^- with H^+ and Zn^{2+} underneath is enhanced, stabilizing the overall system.

Kinetically, H_2 heterolytic dissociation over the Zn−O dimer (path I) must overcome a barrier of 0.55 eV with a reaction energy ΔE of −0.39 eV (exothermic), as plotted in Figure 5C. However, for path II over the Zn−O trench, the barrier becomes 0.20 eV only, despite its less exothermic ΔE of −0.16 eV. The lower barrier for path II can be rationalized partly by its TS (TS1), where the corresponding H−H bond distance of 0.93 Å (Figure 5B) is shorter than that of the path I (0.95 Å, Figure 5A), and a less extent of the H−H stretching and the energy cost is required to reach the TS. These results are consistent with the previous experimental and theoretical study.[31] The weak adsorption and low dissociation energy barrier resulted in the observation of H_2 heterolytic dissociation under cryogenic conditions.

Considering the weak binding of H^- to Zn^{2+}, it might diffuse to the neighbor O^{2-} and become H^+. Calculated diffusion barriers of H^- for paths I and II are 1.05 and 0.96 eV (Figure 5, TS2) along with small ΔE values of 0.15 eV and −0.09, respectively. In addition to the forward diffusion, H^- might recombine with H^+ to form H_2*, and the corresponding barriers are 0.94 eV for path I and 0.36 eV for path II. For the latter one, the barrier for the backward recombination is small and 0.61 eV lower than that for the forward diffusion. This shows that the dissociated H^+ and H^- via path II is only metastable and tends to recombine and desorb in the form of H_2 at elevated temperature. However for path I, though the barrier for the backward recombination remains lower than that for the forward diffusion, their difference is as small as 0.11 eV. In other words, both processes become competitive, and importantly both barriers are considerably higher (0.94 eV at least). This indicates that the dissociated H^+ and H^- species

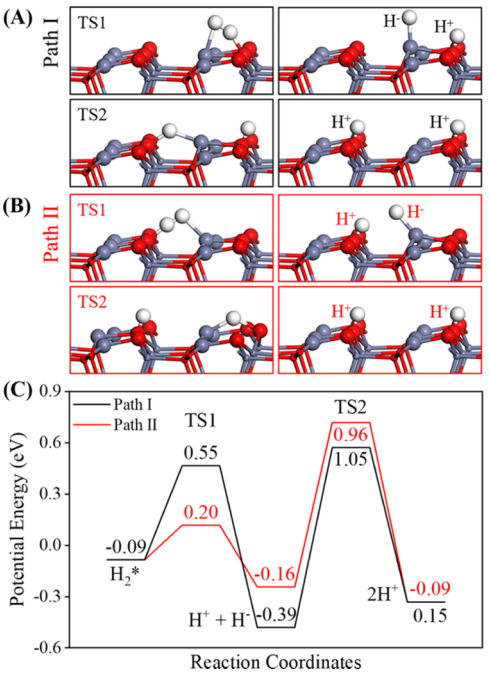

Figure 5. Optimized reaction intermediates and TS structures of H_2 heterolytic dissociation and H^- diffusion over the ZnO(10$\bar{1}$0) surface over (A) Zn−O dimer (path I) and (B) Zn−O trench (path II). Gray, red, and white spheres represent Zn, O, and H atoms, respectively. (C) Corresponding potential energy diagrams. The energy reference zero corresponds to the energy of H_2 in the gas phase and clean surface.

over the O−Zn dimer could have a longer lifetime, and part of the H^- species could diffuse and convert to H^+ at high temperature.

We describe below the change in reactivity when one surface Zn atom was substituted by the Cr atom (noted as Cr_1/ZnO(10$\bar{1}$0) afterward) (Table S1). First, we calculated H_2 dissociation over the Zn−O dimer and Zn−O trench near the Cr_1 atom (Figure 6A). The corresponding dissociation barriers are 0.58 and 0.21 eV along with small exothermic ΔE values of −0.43 and −0.24 eV (Figure 6C), all close to those of the pristine surface. We further investigated the H_2 dissociation over the Cr_1−O dimer and Cr_1−O trench (Figure 6B). It was found that the corresponding dissociation barriers are 0.87 and 0.21 eV along with endothermic ΔE values of 0.19 and 0.12 eV (Figure 6C). These show that the substituted Cr_1 atom shows no improvement in H_2 dissociation. Nevertheless, compared to CO adsorption on the Zn-top with an energy of −0.37 eV, Cr_1 binds CO stronger with −0.52 eV, another important reactant involved in syngas conversion.

3.3. H_2 Activation on Pristine and Zn_1-Substituted Cr_2O_3(001). On Cr_2O_3(001), H_2 molecular adsorption is nearly energetically neutral as found for ZnO(10$\bar{1}$0). The heterolytic dissociation over the Cr−O pair with a bond length of 1.83 Å is investigated, and the calculated dissociative adsorption energy E_{ad} is endothermic and is equal to 0.42 eV/H_2 (Figure 7B). Different from ZnO(10$\bar{1}$0), the lateral interaction between dissociated H^+ and H^- is small because there is little change in the overall energy with infinitely large increase in the corresponding distance. TS1 with a H−H bond distance of 1.11 Å and the corresponding barrier of 0.79 eV is identified as the most favorable TS to dissociate H_2 as shown in Figure 7A. Again, considering the weak binding of H^- to

https://doi.org/10.1021/acs.jpcc.2c02607
J. Phys. Chem. C 2022, 126, 9059−9068

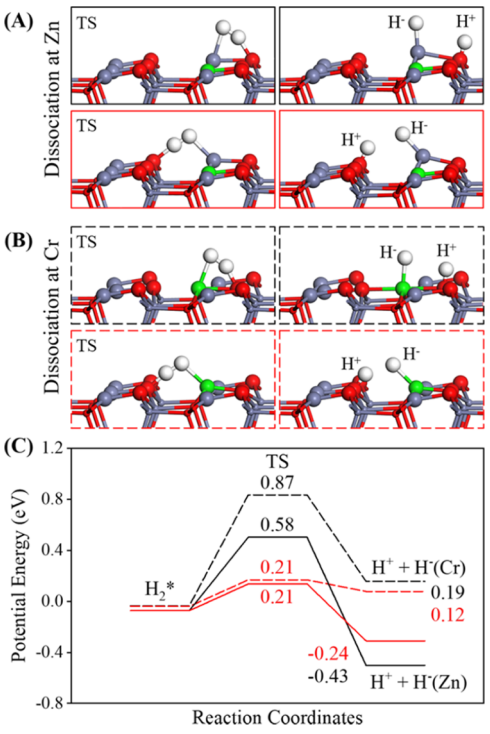

Figure 6. Optimized reaction intermediates and TS structures of H_2 heterolytic dissociation over (A) Zn−O dimer and (B) Cr−O dimer of ZnO(10$\bar{1}$0) with substituted Cr_1. Green, gray, red, and white spheres represent Cr, Zn, O, and H atoms, respectively. (C) Corresponding potential energy diagrams. The energy reference zero corresponds to the energy of H_2 in the gas phase and clean surface.

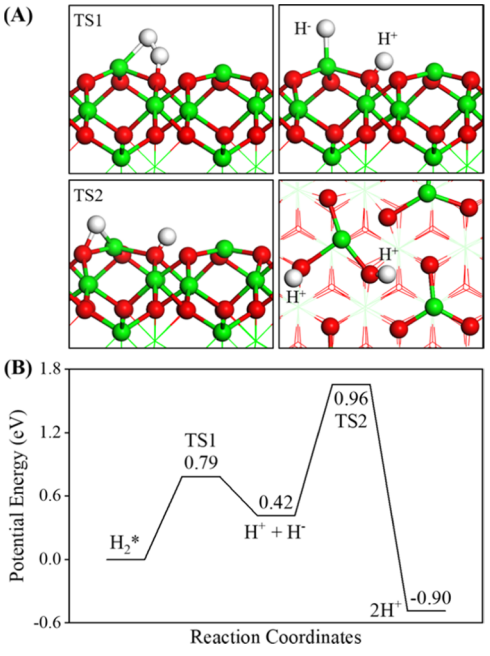

Figure 7. (A) Optimized reaction intermediate configurations, TS structures and (B) potential energy diagrams for H_2 heterolytic dissociation and H^- diffusion over pristine Cr_2O_3(001) surfaces. Green, red, and white spheres represent Cr, O, and H atoms, respectively. The energy reference zero corresponds to the energy of H_2 in the gas phase and clean surface.

Cr^{3+} than H^+ to O^{2-} by 0.60 eV (Figure 2), H^- tends to diffuse to the oxygen nearby and change to H^+. Indeed, the calculated ΔE is −0.90 eV, and the overall ΔE for formation of $2H^+$ afterward with respect to H_2(g) is −0.49 eV/H_2, slightly more exothermic than that of the pristine ZnO(10$\bar{1}$0) (−0.34 eV/H_2). The calculated forward diffusion barrier is as high as 0.96 eV (Figure 7A. TS2). However, the backward recombination barrier for H^- with H^+ to form H_2* is 0.37 eV only. This means that the pristine Cr_2O_3(001) has a rather low activity to dissociate the H_2.

We studied the H_2 heterolytic dissociation on Zn-substituted Cr_2O_3(001), noted as Zn_1/Cr_2O_3(001) here afterward (Figure 8). Again, H_2 molecular adsorption on Zn_1/Cr_2O_3(001) remains neutral. For the Cr−O pairs near the Zn_1(Figure 8A, path I), calculated E_{ad} for the heterolytic dissociation improves considerably and becomes exothermic and is equal to −0.55 eV/H_2. At TS1, the H−H bond distance is 0.96 Å, and the corresponding barrier is 0.63 eV, lower than that of the pristine surface (0.79 eV), due to the improved energetics. The H^- species formed diffuses to the oxygen nearby and becomes H^+ with a considerable ΔE of −1.19 eV. The final structure formed is plotted in Figure 8A, where two H^+ coordinate to two oxygen coordinated to the same Cr cation, and the overall ΔE with respect to H_2(g) is as large as −1.78 eV/H_2. The forward diffusion barrier is 1.35 eV at TS2, slightly higher than its backward recombination barrier of 1.18 eV (Figure 8D). Compared to the pristine surface, the great improvement in energetics and kinetics activates efficiently the Cr−O pairs near the Zn_1 for the H_2 dissociation.

H_2 heterolytic dissociation can take place over the Cr−O long pairs (Figure 2B) with a bond length of 3.28 Å, where the O atom of interest coordinates to the Zn_1 (Figure 8B, path II). The calculated E_{ad} becomes even more exothermic equal to −1.04 eV/H_2. As a result, the corresponding barrier decreases further to 0.21 eV only, and the H−H bond distance at the TS (TS1) is 0.99 Å. After the heterolytic dissociation, H^- formed diffuses to the oxygen nearby and becomes H^+ with a modest ΔE of −0.62 eV. The final structure formed is plotted in Figure 8B, where one H^+ from dissociation coordinates to the oxygen coordinated to Zn_1, and another H^+ from diffusion coordinates to the oxygen coordinated to Cr, and the overall ΔE with respect to H_2(g) is also significantly −1.70 eV/H_2. The forward diffusion barrier to form $2H^+$ is 1.39 eV at TS2, which is slightly higher than its backward recombination barrier of 1.26 eV to form H_2*. Similar to the Cr−O pairs near the Zn_1, the Cr−O long pairs nearby are active for the H_2 dissociation as well.

H_2 dissociation adsorption over the Zn_1−O pairs with a bond length of 1.86 Å was also studied (Figure 8C, path III), and the calculated E_{ad} was slightly exothermic equal to −0.22 eV/H_2, close to that of the pristine ZnO(10$\bar{1}$0) despite their different local coordination. At TS1, the H−H bond distance is 0.98 Å, and the corresponding barrier is 0.63 eV. The H^- species formed diffuses to the oxygen coordinated with the Zn_1 and becomes H^+ with a significant ΔE of −1.40 eV. The final structure formed is plotted in Figure 8C, where two H^+ coordinates to two oxygen coordinated to the same Zn_1, and the overall ΔE with respect to H_2 (g) is −1.66 eV/H_2. The diffusion barrier at TS2 is 0.63 eV, smaller than that of the pristine ZnO(10$\bar{1}$0) largely due to the improved energetics. Importantly, the forward diffusion barrier is lower than the backward recombination barrier of 0.85 eV to form H_2*.

https://doi.org/10.1021/acs.jpcc.2c02607
J. Phys. Chem. C 2022, 126, 9059−9068

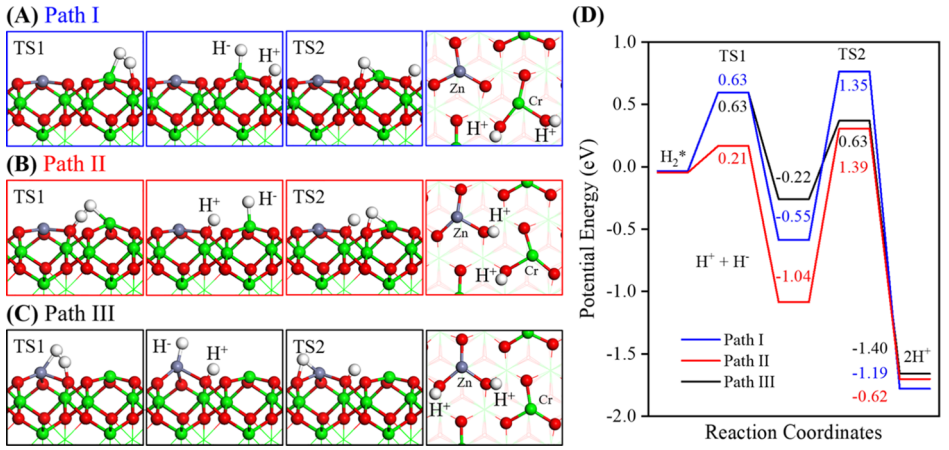

Figure 8. Optimized reaction intermediates and TS structures of H_2 heterolytic dissociation and H^- diffusion over $Cr_2O_3(001)$ with substituted Zn_1 over (A) Cr−O pair (path I), (B) Cr−O long pair (path II), and (C) Zn_1−O pair (path III). Green, gray, red, and white spheres represent Cr, Zn, O, and H atoms, respectively. (D) Corresponding potential energy diagrams. The energy reference zero corresponds to the energy of H_2 in the gas phase and clean surface.

Namely, the Zn_1−O pairs on the $Zn_1/Cr_2O_3(001)$ are also active to dissociate the H_2 molecule.

Above investigations show clearly that the presence of the low-valent Zn_1 not only promotes the H_2 heterolytic dissociation but also the formation of the homolytic H^+ and two lattice hydroxyl groups finally. Higher reactivity comes from the improved reactivity of the lattice oxygen with a lower vacancy formation energy E_V. We rationalize this using the improved ΔE for the heterolytic dissociation forming H^- and H^+ over the Cr/Zn_1−O pairs, respectively. When the Zn_1 is introduced, there is little change in the binding strength of H^- to the Cr cation nearby (less than 0.02 eV). Moreover, the binding strength of H^- to the Zn_1 cation is also close to that of the pristine ZnO(10$\bar{1}$0), different by 0.15 eV only. Namely, the cations have no contribution to the increased reactivity. In contrast, the binding strength of H^+ to the oxygen coordinated to the Cr near the Zn_1 (path I) increases considerably by 0.85 eV, changing the dissociation from endothermic to exothermic. This can be understood by a decrease in the corresponding E_V from 4.14 eV (the pristine surface) to 3.28 eV. For path II, the binding strength of H^+ to the oxygen coordinated to the Zn_1 enhances by1.45 eV along with the least E_V of 3.03 eV, and the corresponding dissociation process becomes most exothermic. Path III is different from path II by H^- coordinating to the Zn_1 rather than the Cr. The binding strength of H^- to the Zn_1 is 0.91 eV weaker than that to the Cr, increasing the overall energetics but remaining more favorable than that of the pristine $Cr_2O_3(001)$, as plotted in Figures 8C and 7B.

3.4. Influence on Reducibility and Dehydration. Hydrogen molecules might react with the oxide surfaces by forming water with oxygen vacancies left, which is studied below. Calculated ΔE between $H_2(g)$ and the lattice oxygen to form $H_2O(g)$ is endothermic by 0.30 eV on the pristine ZnO(10$\bar{1}$0) but highly endothermic by 1.60 eV on the pristine $Cr_2O_3(001)$. Namely, ZnO(10$\bar{1}$0) is much easier reduced than $Cr_2O_3(001)$, consistent with their different E_V of 2.83 and 4.14 eV, respectively. At higher temperatures, the corresponding free energy becomes exothermic, and the oxide surfaces would be reduced. For Cr_1/ZnO(10$\bar{1}$0), the oxygen coordinated to the high-valent Cr_1 is stabilized and becomes more resistant to the reduction, and the calculated ΔE becomes highly endothermic by 1.36 eV. For the oxygen nearby but not coordinated to the Cr_1, corresponding ΔE is 0.47 eV, remaining close to that of the pristine ZnO. This shows that the Cr_1 worsens the reducibility of ZnO(10$\bar{1}$0), but this happens only on the Cr_1-coordinated oxygen. For $Zn_1/Cr_2O_3(001)$, the oxygen coordinated to the low-valent Zn_1 is destabilized and prone to be reduced for its small ΔE of 0.68 eV. Moreover, we found that for the oxygen nearby but not coordinated to Zn_1, corresponding ΔE also becomes modest varying from 0.49 to 0.75 eV. In other words, the Zn_1 enhances the reducibility of $Cr_2O_3(001)$, and the influence is not limited to the Zn_1-coordinated oxygen but also the oxygen nearby.

To see the kinetics of reduction and eventually formation of water, we start from ZnO(10$\bar{1}$0). There are two possible reaction pathways, and the first one is the direct pathway from H^+ and H^- (Figure 5). The H^+ species bond with the surface oxygen to form the lattice hydroxyl (HO*), which could be attacked by the H^- species to form H_2O*. However, irrespective of the reaction path over either the Zn−O dimer (path I) or the Zn−O trench (path II) (Figure 9A), corresponding processes to form a lattice H_2O*-like intermediate sitting in the oxygen vacancy O_v are highly endothermic by 1.31 and 1.08 eV (Figure 9B). This comes mainly from the strong electrostatic repulsion when H^- approaches the negatively charged O of the lattice HO* and considerable energy cost for bending of the H^-−Zn bond. Therefore, though subsequent water formation (Figure 9C) is an energetically downhill process with a small barrier, significant reaction barriers (1.50 and 1.93 eV) and endothermic features in the previous step prevent the pathway.

Alternatively, water could be produced by two lattice HO* (or equivalent $2H^+$ as plotted in Figure 10A), where one is formed directly during the H_2 heterolytic dissociation, and another one is formed via diffusion of the H^- species to the lattice oxygen. To form water, one lattice HO* first migrates out from the lattice and sits at the bridge site of the Zn (Figure 10A). The corresponding ΔE is endothermic by 0.20 eV along with a barrier of 0.75 eV at TS1. Then, the bridge HO* reacts with H^+ of the lattice HO* to form H_2O* with a ΔE and a barrier of −0.34 eV (exothermic) and 0.14 eV at TS2, respectively. Finally, desorption of H_2O* into the gas phase costs 0.77 eV. Throughout the entire process, the rate-determining step is diffusion of the H^- species with a barrier of

https://doi.org/10.1021/acs.jpcc.2c02607
J. Phys. Chem. C 2022, 126, 9059−9068

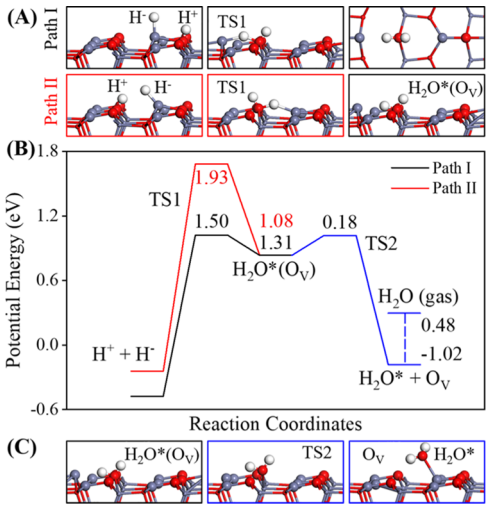

Figure 9. Optimized reaction intermediates and TS structures of surface reduction to form H_2O via H^- attacking the lattice HO* via (A) path I and (B) path II over the ZnO(10$\bar{1}$0) surface. (B) Corresponding potential energy diagrams. (C) Optimized reaction intermediates and TS structures of H_2O^* diffusion with an oxygen vacancy O_V left. The energy reference zero corresponds to the energy of H_2 in the gas phase and clean surface.

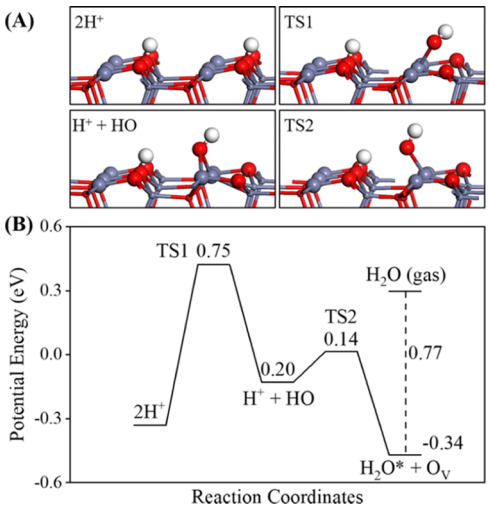

Figure 10. (A) Optimized reaction intermediate configurations, TS structures, and (B) potential energy diagrams for ZnO(10$\bar{1}$0) reduction to form H_2O via the lattice hydroxyls. The energy reference zero corresponds to the energy of H_2 in the gas phase and clean surface.

1.05 eV. As shown in Figure 5, this diffusion competes with recombination to form H_2, therefore H_2 reduction to form H_2O is limited at the low coverage considered. When the Cr_1 is introduced, dehydration is suppressed as seen from the above energetics and not discussed explicitly here.

Formation of water via the H_2 reduction on Cr_2O_3(001) is energetically rather unfavorable as indicated above. Therefore, we look at the Zn_1/Cr_2O_3(001). We note that though the domain around the Zn_1 sites could be reduced by the H_2, the direct process via the H^- species attacking the lattice HO* was unlikely as found in the pristine ZnO(10$\bar{1}$0). For the water formation via two lattice HO*, Figure 8 shows that the lattice HO* formed via the H_2 dissociation is very stable. Subsequent water formation becomes highly endothermic by more than 2 eV. As a result, the reactivity of dehydration from the H_2 dissociation on the pristine and Zn_1-substituted Cr_2O_3(001) is lower than that on the pristine and Cr_1-substituted ZnO(10$\bar{1}$0).

4. CONCLUSIONS

Comprehensive DFT calculations are performed to study H_2 activation over the pristine and substituted ZnO(10$\bar{1}$0) and Cr_2O_3(001). It is found that Cr_1-substituted ZnO(10$\bar{1}$0) and Zn_1-substituted Cr_2O_3(001) are stable in a wide range of temperatures and pressures considered. For hydrogen binding to the lattice oxygen of ZnO(10$\bar{1}$0), the electrons are delocalized on the whole surface but become localized in the Cr−O bond for Cr_2O_3(001). On both surfaces, H_2 heterolytic dissociation is found to be more favorable than the homolytic one. On ZnO(10$\bar{1}$0), the H_2 heterolytic dissociation occurs over the Zn−O dimer instead of the Zn−O trench, and afterward the hydride species formed tends to diffuse to the nearby lattice oxygen forming a hydroxyl group. Cr_1 substitution on ZnO(10$\bar{1}$0) has little improvement in H_2 activation. The pristine Cr_2O_3(001) is less active for H_2 dissociation. However, when one surface Cr cation is substituted by Zn_1, the domain around the substitutional sites efficiently promotes the H_2 heterolytic dissociation and subsequent migration of the hydride to form a hydroxyl group. At elevated temperatures, the dissociated H species tend to recombine and form hydrogen molecules, rather than reacting with the lattice oxygen to form water.

■ ASSOCIATED CONTENT

Supporting Information

The Supporting Information is available free of charge at https://pubs.acs.org/doi/10.1021/acs.jpcc.2c02607.

Detailed structure configurations (PDF)

■ AUTHOR INFORMATION

Corresponding Author

Wei-Xue Li − *Department of Chemical Physics, School of Chemistry and Materials Science, University of Science and Technology of China, Hefei, Anhui 230026, China; Hefei National Research Center for Physical Science at the Microscale, Hefei, Anhui 230026, China;* orcid.org/0000-0002-5043-3088; Email: wxli70@ustc.edu.cn

Authors

Jie Luo − *Department of Chemical Physics, School of Chemistry and Materials Science, University of Science and Technology of China, Hefei, Anhui 230026, China;* orcid.org/0000-0002-0932-8331

Jin-Xun Liu − *Department of Chemical Physics, School of Chemistry and Materials Science, University of Science and Technology of China, Hefei, Anhui 230026, China;* orcid.org/0000-0002-7499-4197

Complete contact information is available at: https://pubs.acs.org/10.1021/acs.jpcc.2c02607

Notes

The authors declare no competing financial interest.

■ ACKNOWLEDGMENTS

This work was supported by the Key Technologies R&D Program of China (2018YFA0208603), the National Natural

Science Foundation of China (91645202, 91945302), the start-up funds of University of Science and Technology of China (KY2060000171), USTC Research Funds of the Double First-Class Initiative (YD2060002012), and the high-performance computational resources provided by University of Science and Technology of China.

REFERENCES

(1) Rostrup-Nielsen, J. R. Production of synthesis gas. *Catal. Today* **1993**, *18*, 305−324.
(2) Bharadwaj, S. S.; Schmidt, L. D. Catalytic partial oxidation of natural gas to syngas. *Fuel Process. Technol.* **1995**, *42*, 109−127.
(3) Edwards, J. H.; Maitra, A. M. The chemistry of methane reforming with carbon dioxide and its current and potential applications. *Fuel Process. Technol.* **1995**, *42*, 269−289.
(4) Shoko, E.; McLellan, B.; Dicks, A. L.; da Costa, J. C. D. Hydrogen from coal: Production and utilisation technologies. *Int. J. Coal Geol.* **2006**, *65*, 213−222.
(5) Göransson, K.; Söderlind, U.; He, J.; Zhang, W. Review of syngas production via biomass DFBGs. *Renewable Sustainable Energy Rev.* **2011**, *15*, 482−492.
(6) Jiao, F.; Li, J.; Pan, X.; Xiao, J.; Li, H.; Ma, H.; Wei, M.; Pan, Y.; Zhou, Z.; Li, M.; Miao, S.; Li, J.; Zhu, Y.; Xiao, D.; He, T.; Yang, J.; Qi, F.; Fu, Q.; Bao, X. Selective conversion of syngas to light olefins. *Science* **2016**, *351*, 1065−1068.
(7) Cheng, K.; Gu, B.; Liu, X.; Kang, J.; Zhang, Q.; Wang, Y. Direct and Highly Selective Conversion of Synthesis Gas into Lower Olefins: Design of a Bifunctional Catalyst Combining Methanol Synthesis and Carbon−Carbon Coupling. *Angew. Chem., Int. Ed.* **2016**, *55*, 4725−4728.
(8) Liu, X.; Wang, M.; Yin, H.; Hu, J.; Cheng, K.; Kang, J.; Zhang, Q.; Wang, Y. Tandem Catalysis for Hydrogenation of CO and CO_2 to Lower Olefins with Bifunctional Catalysts Composed of Spinel Oxide and SAPO-34. *ACS Catal.* **2020**, *10*, 8303−8314.
(9) Tan, L.; Wang, F.; Zhang, P.; Suzuki, Y.; Wu, Y.; Chen, J.; Yang, G.; Tsubaki, N. Design of a core−shell catalyst: an effective strategy for suppressing side reactions in syngas for direct selective conversion to light olefins. *Chem. Sci.* **2020**, *11*, 4097−4105.
(10) Li, N.; Jiao, F.; Pan, X.; Chen, Y.; Feng, J.; Li, G.; Bao, X. High-Quality Gasoline Directly from Syngas by Dual Metal Oxide−Zeolite (OX-ZEO) Catalysis. *Angew. Chem., Int. Ed.* **2019**, *58*, 7400−7404.
(11) Su, J.; Wang, D.; Wang, Y.; Zhou, H.; Liu, C.; Liu, S.; Wang, C.; Yang, W.; Xie, Z.; He, M. Direct Conversion of Syngas into Light Olefins over Zirconium-Doped Indium(III) Oxide and SAPO-34 Bifunctional Catalysts: Design of Oxide Component and Construction of Reaction Network. *ChemCatChem* **2018**, *10*, 1536−1541.
(12) Zhou, W.; Cheng, K.; Kang, J.; Zhou, C.; Subramanian, V.; Zhang, Q.; Wang, Y. New horizon in C1 chemistry: breaking the selectivity limitation in transformation of syngas and hydrogenation of CO_2 into hydrocarbon chemicals and fuels. *Chem. Soc. Rev.* **2019**, *48*, 3193−3228.
(13) Arslan, M. T.; Qureshi, B. A.; Gilani, S. Z. A.; Cai, D.; Ma, Y.; Usman, M.; Chen, X.; Wang, Y.; Wei, F. Single-Step Conversion of H_2-Deficient Syngas into High Yield of Tetramethylbenzene. *ACS Catal.* **2019**, *9*, 2203−2212.
(14) Miao, D.; Ding, Y.; Yu, T.; Li, J.; Pan, X.; Bao, X. Selective Synthesis of Benzene, Toluene, and Xylenes from Syngas. *ACS Catal.* **2020**, *10*, 7389−7397.
(15) Liu, X.; Zhou, W.; Yang, Y.; Cheng, K.; Kang, J.; Zhang, L.; Zhang, G.; Min, X.; Zhang, Q.; Wang, Y. Design of efficient bifunctional catalysts for direct conversion of syngas into lower olefins via methanol/dimethyl ether intermediates. *Chem. Sci.* **2018**, *9*, 4708−4718.
(16) Fu, X.; Li, J.; Long, J.; Guo, C.; Xiao, J. Understanding the Product Selectivity of Syngas Conversion on ZnO Surfaces with Complex Reaction Network and Structural Evolution. *ACS Catal.* **2021**, *11*, 12264−12273.
(17) Chen, S.; Ma, S.; Liu, Z.-P. Zirconia-Supported ZnO Single Layer for Syngas Conversion Revealed from Machine-Learning Atomic Simulation. *J. Phys. Chem. Lett.* **2021**, *12*, 3328−3334.
(18) Lai, Z.; Sun, N.; Jin, J.; Chen, J.; Wang, H.; Hu, P. Resolving the Intricate Mechanism and Selectivity of Syngas Conversion on Reduced $ZnCr_2O_x$: A Quantitative Study from DFT and Microkinetic Simulations. *ACS Catal.* **2021**, *11*, 12977−12988.
(19) Ferrin, P.; Kandoi, S.; Nilekar, A. U.; Mavrikakis, M. Hydrogen adsorption, absorption and diffusion on and in transition metal surfaces: A DFT study. *Surf. Sci.* **2012**, *606*, 679−689.
(20) Wang, H.; Nie, X.; Guo, X.; Song, C. A computational study of adsorption and activation of CO_2 and H_2 over Fe(100) surface. *J. CO_2 Util.* **2016**, *15*, 107−114.
(21) van Steen, E.; van Helden, P. A DFT study of hydrogen dissociation on CO-and C-precovered Fe(100) surfaces. *J. Phys. Chem. C* **2010**, *114*, 5932−5940.
(22) Chen, Q.; Svenum, I.-H.; Gavrilovic, L.; Chen, D.; Blekkan, E. A. Effect of trace potassium on hydrogen adsorption and dissociation on hcp cobalt: A density functional theory study. *Surf. Sci.* **2019**, *681*, 24−31.
(23) Yu, M.; Liu, L.; Wang, Q.; Jia, L.; Hou, B.; Si, Y.; Li, D.; Zhao, Y. High coverage H_2 adsorption and dissociation on fcc Co surfaces from DFT and thermodynamics. *Int. J. Hydrogen Energy* **2018**, *43*, 5576−5590.
(24) van Helden, P.; van den Berg, J.-A.; Weststrate, C. J. Hydrogen adsorption on Co surfaces: a density functional theory and temperature programmed desorption study. *ACS Catal.* **2012**, *2*, 1097−1107.
(25) Wijzenbroek, M.; Kroes, G. J. The effect of the exchange-correlation functional on H_2 dissociation on Ru(0001). *J. Chem. Phys.* **2014**, *140*, 084702.
(26) Luppi, M.; Olsen, R. A.; Baerends, E. J. Six-dimensional potential energy surface for H_2 at Ru(0001). *Phys. Chem. Chem. Phys.* **2006**, *8*, 688−696.
(27) Díaz, C.; Pijper, E.; Olsen, R. A.; Busnengo, H. F.; Auerbach, D. J.; Kroes, G. J. Chemically accurate simulation of a prototypical surface reaction: H_2 dissociation on Cu(111). *Science* **2009**, *326*, 832−834.
(28) Wang, S.-S.; Su, H.-Y.; Gu, X.-K.; Li, W.-X. Differentiating Intrinsic Reactivity of Copper, Copper−Zinc Alloy, and Copper/Zinc Oxide Interface for Methanol Steam Reforming by First-Principles Theory. *J. Phys. Chem. C* **2017**, *121*, 21553−21559.
(29) Wu, X.-K.; Xia, G.-J.; Huang, Z.; Rai, D. K.; Zhao, H.; Zhang, J.; Yun, J.; Wang, Y.-G. Mechanistic insight into the catalytically active phase of CO_2 hydrogenation on Cu/ZnO catalyst. *Appl. Surf. Sci.* **2020**, *525*, 146481.
(30) García-Melchor, M.; López, N. Homolytic products from heterolytic paths in H_2 dissociation on metal oxides: the example of CeO_2. *J. Phys. Chem. C* **2014**, *118*, 10921−10926.
(31) Shi, H.; Yuan, H.; Li, Z.; Wang, W.; Li, Z.; Shao, X. Low-Temperature Heterolytic Adsorption of H_2 on ZnO($10\bar{1}0$) Surface. *J. Phys. Chem. C* **2019**, *123*, 13283−13287.
(32) Anderson, A. B.; Nichols, J. A. Hydrogen on zinc oxide. Theory of its heterolytic adsorption. *J. Am. Chem. Soc.* **1986**, *108*, 4742−4746.
(33) Wang, Y.; Meyer, B.; Yin, X.; Kunat, M.; Langenberg, D.; Traeger, F.; Birkner, A.; Wöll, C. Hydrogen Induced Metallicity on the ZnO($10\bar{1}0$) Surface. *Phys. Rev. Lett.* **2005**, *95*, 266104.
(34) Lopes Martins, J. B.; Longo, E.; Rodríguez Salmon, O. D.; Espinoza, V. A. A.; Taft, C. A. The interaction of H_2, CO, CO_2, H_2O and NH_3 on ZnO surfaces: an Oniom Study. *Chem. Phys. Lett.* **2004**, *400*, 481−486.
(35) Mun, B. S.; Liu, Z.; Motin, M. A.; Roy, P. C.; Kim, C. M. In situ observation of H_2 dissociation on the ZnO (0001) surface under high pressure of hydrogen using ambient-pressure XPS. *Int. J. Hydrogen Energy* **2018**, *43*, 8655−8661.
(36) Conner, W.; Kokes, R. J. Hydrogen activation on zinc oxide. *J. Catal.* **1975**, *36*, 199−210.

https://doi.org/10.1021/acs.jpcc.2c02607
J. Phys. Chem. C 2022, 126, 9059−9068

(37) Gu, X.-K.; Qiao, B.; Huang, C.-Q.; Ding, W.-C.; Sun, K.; Zhan, E.; Zhang, T.; Liu, J.; Li, W.-X. Supported Single Pt_1/Au_1 Atoms for Methanol Steam Reforming. *ACS Catal.* **2014**, *4*, 3886−3890.
(38) Kumar, A.; Ropital, F.; de Bruin, T.; Diawara, B. Effects of surface orientations of Cr_2O_3 on CO_2 adsorption: A DFT approach. *Appl. Surf. Sci.* **2020**, *529*, 147127.
(39) Maldonado, F.; Stashans, A. DFT modelling of hydrogen sulphide adsorption on α-Cr_2O_3(0001) surface. *Surf. Sci.* **2016**, *647*, 78−83.
(40) Jin, J.; Sun, N.; Hu, W.; Yuan, H.; Wang, H.; Hu, P. Insight into Room-Temperature Catalytic Oxidation of Nitric oxide by Cr_2O_3: A DFT Study. *ACS Catal.* **2018**, *8*, 5415−5424.
(41) Ng, M. F.; Blackwood, D. J.; Jin, H.; Tan, T. L. Tuning oxygen reduction activity on chromia surface via alloying: a DFT study. *Chem.—Asian J.* **2020**, *15*, 4087−4092.
(42) Kresse, G.; Furthmüller, J. Efficiency of ab-initio total energy calculations for metals and semiconductors using a plane-wave basis set. *Comput. Mater. Sci.* **1996**, *6*, 15−50.
(43) Kresse, G.; Furthmüller, J. Efficient iterative schemes forab initiototal-energy calculations using a plane-wave basis set. *Phys. Rev. B* **1996**, *54*, 11169−11186.
(44) Blöchl, P. E. Projector augmented-wave method. *Phys. Rev. B* **1994**, *50*, 17953−17979.
(45) Kresse, G.; Joubert, D. From ultrasoft pseudopotentials to the projector augmented-wave method. *Phys. Rev. B* **1999**, *59*, 1758−1775.
(46) Perdew, J. P.; Burke, K.; Ernzerhof, M. Generalized Gradient Approximation Made Simple. *Phys. Rev. Lett.* **1996**, *77*, 3865−3868.
(47) Meyer, B.; Rabaa, H.; Marx, D. Water adsorption on ZnO($10\bar{1}0$): from single molecules to partially dissociated monolayers. *Phys. Chem. Chem. Phys.* **2006**, *8*, 1513−1520.
(48) Pala, R.; Metiu, H. Selective promotion of different modes of methanol adsorption via the cation substitutional doping of a ZnO($10\bar{1}0$) surface. *J. Catal.* **2008**, *254*, 325−331.
(49) Gu, X.-K.; Huang, C.-Q.; Li, W.-X. First-principles study of single transition metal atoms on ZnO for the water gas shift reaction. *Catal. Sci. Technol.* **2017**, *7*, 4294−4301.
(50) Escudero, R.; Escamilla, R. Ferromagnetic behavior of high-purity ZnO nanoparticles. *Solid State Commun.* **2011**, *151*, 97−101.
(51) Abrahams, S. C.; Bernstein, J. L. Remeasurement of the structure of hexagonal ZnO. *Acta Crystallogr., Sect. B: Struct. Crystallogr. Cryst. Chem.* **1969**, *25*, 1233−1236.
(52) Dronskowski, R.; Bloechl, P. E. Crystal Orbital Hamilton Populations (COHP). Energy-Resolved Visualization of Chemical Bonding in Solids Based on Density-Functional Calculations. *J. Phys. Chem.* **1993**, *97*, 8617−8624.
(53) Deringer, V. L.; Tchougréeff, A. L.; Dronskowski, R. Crystal orbital Hamilton population (COHP) analysis as projected from plane-wave basis sets. *J. Phys. Chem. A* **2011**, *115*, 5461−5466.
(54) Maintz, S.; Deringer, V. L.; Tchougréeff, A. L.; Dronskowski, R. Analytic projection from plane-wave and PAW wavefunctions and application to chemical-bonding analysis in solids. *J. Comput. Chem.* **2013**, *34*, 2557−2567.
(55) Maintz, S.; Deringer, V. L.; Tchougréeff, A. L.; Dronskowski, R. LOBSTER: A tool to extract chemical bonding from plane-wave based DFT. *J. Comput. Chem.* **2016**, *37*, 1030−1035.
(56) Maldonado, F.; Novillo, C.; Stashans, A. Ab initio calculation of chromium oxide containing Ti dopant. *Chem. Phys.* **2012**, *393*, 148−152.
(57) Shi, S.; Wysocki, A. L.; Belashchenko, K. D. Magnetism of chromia from first-principles calculations. *Phys. Rev. B* **2009**, *79*, 104404.
(58) Mosey, N. J.; Liao, P.; Carter, E. A. Rotationally invariant ab initio evaluation of Coulomb and exchange parameters for DFT+U calculations. *J. Chem. Phys.* **2008**, *129*, 014103.
(59) Rohrbach, A.; Hafner, J.; Kresse, G. Ab initio study of the (0001) surfaces of hematite and chromia: Influence of strong electronic correlations. *Phys. Rev. B* **2004**, *70*, 125426.
(60) Golosova, N. O.; Kozlenko, D. P.; Kichanov, S. E.; Lukin, E. V.; Liermann, H.-P.; Glazyrin, K. V.; Savenko, B. N. Structural and magnetic properties of Cr_2O_3 at high pressure. *J. Alloys Compd.* **2017**, *722*, 593−598.
(61) Baster, M.; Bourée, F.; Kowalska, A.; Latacz, Z. The change of crystal and exchange parameters in the vicinity of TN in Cr_2O_3. *J. Alloys Compd.* **2000**, *296*, 1−5.
(62) Finger, L. W.; Hazen, R. M. Crystal structure and isothermal compression of Fe_2O_3, Cr_2O_3, and V_2O_3 to 50 kbars. *J. Appl. Phys.* **1980**, *51*, 5362−5367.
(63) Henkelman, G.; Jónsson, H. Improved tangent estimate in the nudged elastic band method for finding minimum energy paths and saddle points. *J. Chem. Phys.* **2000**, *113*, 9978−9985.
(64) Li, W.-X.; Stampfl, C.; Scheffler, M. Why is a Noble Metal Catalytically Active? The Role of the O-Ag Interaction in the Function of Silver as an Oxidation Catalyst. *Phys. Rev. Lett.* **2003**, *90*, 256102.
(65) Reuter, K.; Scheffler, M. Composition, structure, and stability of RuO_2(110) as a function of oxygen pressure. *Phys. Rev. B* **2001**, *65*, 035406.
(66) Wang, V.; Xu, N.; Liu, J.-C.; Tang, G.; Geng, W.-T. VASPKIT: A user-friendly interface facilitating high-throughput computing and analysis using VASP code. *Comput. Phys. Commun.* **2021**, *267*, 108033.
(67) Yin, X.-L.; Birkner, A.; Hänel, K.; Löber, T.; Köhler, U.; Wöll, C. Adsorption of atomic hydrogen on ZnO($10\bar{1}0$): STM study. *Phys. Chem. Chem. Phys.* **2006**, *8*, 1477−1481.
(68) Kováčik, R.; Meyer, B.; Marx, D. F Centers versus Dimer Vacancies on ZnO Surfaces: Characterization by STM and STS Calculations. *Angew. Chem., Int. Ed.* **2007**, *46*, 4894−4897.
(69) Huang, W.; Cai, J.; Hu, J.; Zhu, J.; Yang, F.; Bao, X. Atomic structures and electronic properties of Cr-doped ZnO($10\bar{1}0$) surfaces. *Chin. J. Catal.* **2021**, *42*, 971−979.
(70) Harris, J.; Andersson, S. H_2 dissociation at metal surfaces. *Phys. Rev. Lett.* **1985**, *55*, 1583.
(71) Lischka, M.; Groß, A. Hydrogen adsorption on an open metal surface: H_2/Pd(210). *Phys. Rev. B: Condens. Matter Mater. Phys.* **2002**, *65*, 075420.
(72) Scarano, D.; Spoto, G.; Bordiga, S.; Zecchina, A.; Lamberti, C. Lateral interactions in CO adlayers on prismatic ZnO faces: a FTIR and HRTEM study. *Surf. Sci.* **1992**, *276*, 281−298.
(73) Diebold, U.; Koplitz, L.; Dulub, O. Atomic-scale properties of low-index ZnO surfaces. *Appl. Surf. Sci.* **2004**, *237*, 336−342.
(74) Wang, X.-G.; Smith, J. R. Surface phase diagram for Cr_2O_3(0001): Ab initio density functional study. *Phys. Rev. B: Condens. Matter Mater. Phys.* **2003**, *68*, 201402.

https://doi.org/10.1021/acs.jpcc.2c02607
J. Phys. Chem. C 2022, 126, 9059−9068